

EXPERIMENTAL TEMPERATURE ANALYSIS OF POWDER-BASED ELECTRON BEAM ADDITIVE MANUFACTURING

Steven Price*, James Lydon**, Ken Cooper**, Kevin Chou*

*Department of Mechanical Engineering
The University of Alabama, Tuscaloosa, AL 35487, USA

**Advanced Manufacturing Technology Team
Marshall Space Flight Center, Huntsville, AL 35812, USA

Accepted August 16th 2013

Abstract

A near infrared thermal imager has been employed for temperature measurements (build part surfaces) in the powder-based electron beam additive manufacturing (EBAM) process. A methodology has also been developed to analyze temperature distributions and history around the melting scan area. The temperature profiles along the beam scanning clearly show the moving source of heat phenomenon, with the peak temperature reaching over 2000 °C (for Ti-6Al-4V) followed by extremely rapid cooling opposite to the beam scanning direction, except a slow-cooling portion corresponding to the liquidus-solidus range. The build surface temperatures and the melt pool sizes, in the localized electron beam scanning area, were studied at various configurations, e.g., different build heights, also with or without an overhang.

Introduction

Additive manufacturing (AM) is a fabrication technique that creates parts layer by layer based on geometry defined by computer-aided design (CAD) software. Many different methodologies of AM exist such as fused deposition modeling, stereolithography, and selective laser sintering. Some types produce plastic parts while others are capable of fabricating metal parts. Several benefits of AM are rapid production time, capability to produce complex geometry, and no tooling (Gong et al., 2012) [1].

Electron beam additive manufacturing is an AM technology that uses an electron beam to melt cross-sections of a part layer after layer in a metal powder such as Ti-6Al-4V. EBAM is capable of producing high strength, full density metal parts unlike other AM methods such as selective laser sintering. Because of its high energy density, the EBAM fabrication process is much faster than alternatives such as direct laser melting. EBAM enables the fabrication of metal parts with complex geometries such as fine network structures and internal channels and cavities that are difficult to produce using conventional manufacturing methods (Gong et al., 2012) [1].

The EBAM build process consists of pre-heating, contour melting, and hatch melting phases. The pre-heating phase elevates the temperature of the powder in order to reduce the thermal gradient experienced during melting, thereby reducing residual stresses. Contour melting is accomplished by multiple electron beams that melt the boundary of the cross section being created. Hatch melting is performed by a single electron beam scanning a raster pattern in

order to melt the powder that will become the interior of the part. A new layer of powder is then distributed over the build platform in preparation for the next layer's fabrication.

The ability to measure the temperatures that occur during the build process is an essential capability that must be established in order to verify process models, predict part microstructure, and develop feedback control systems. Thermocouples and many types of infrared cameras have been used to measure process temperatures in various types of AM processes. Zäh and Lutzmann (2012) [2] used a thermocouple to measure the temperature 0.3 mm below the powder layer during an EBAM process. Qian et al. (2005) [3] used four Type K thermocouples and three Type W thermocouples to monitor temperatures in the substrate and the part interior during material deposition during a direct laser fabrication (DLF) process. Thermocouples, however, tend to have several limitations in their effectiveness at monitoring process temperatures in additive manufacturing. Because additive manufacturing involves a fast, transient heat source, the limited spatial temperature resolution and slow response time of thermocouples limit their usefulness when monitoring AM processes.

Non-contact infrared imagers have been widely utilized in AM temperature measurement because of their excellent spatial temperature resolution and fast response time. Wegner and Witt (2011) [4] used an InfraTec Jade III MWIR thermal imaging system with a spectral range of 3-5 μm , a resolution of 320 x 240 pixels, and a frame rate of 700 Hz to measure the temperature distribution during a laser sintering process. Infrared cameras sensitive in the near-infrared spectrum (0.8-2.5 μm) are better suited for measuring high temperatures (>1000 K) and also provide the benefit of being less sensitive to surface emissivity. Craeghs et al. (2011) [5] used a high-speed NIR CMOS camera and a photodiode sensor that were both sensitive to the spectral range of 0.7-0.95 μm to monitor the size of the molten pool during a layer-wise laser melting process. Wang et al. (2009) [6] used a Thermaviz two-wavelength imaging pyrometer system sensitive in the 0.7-0.8 μm and 0.8-0.9 μm wavelengths and a detectable temperature range of 1450-1860 $^{\circ}\text{C}$ to measure the temperatures and molten pool shape during a LENS process.

Recently, there have been a few attempts for the use of infrared cameras to measure temperatures during the EBAM process. Schwerdtfeger et al. (2012) [7] used a FLIR A320 IR camera with a resolution of 320 x 240 pixels and a spatial resolution of 0.83 mm per pixel to detect flaws during an EBAM process. In order to avoid the metallization of the camera's viewport, a mechanical shutter was used to cover the viewport during the melting sequence. The shutter was then opened immediately after the layer's melting sequence was completed so the IR camera could capture images. The captured IR images had a low resolution; however the general locations of flaws were detectable. Rodriguez et al. (2012) [8] used a FLIR SC635 IR camera with a resolution of 640 x 480 pixels and a spatial resolution of 350 μm per pixel as part of a feedback control system for an Arcam A2 EBAM system. They also used a shutter to shield the camera-port during the melting sequence, opening it for viewing once the melting was finished. Non-uniform temperature distributions were easily identified with the IR camera. An issue in determining accurate relative temperatures seen by both Schwerdtfeger et al. [7] and Rodriguez et al. [8] was the apparent "cold spots" that can be caused either by lower temperatures or lower surface emissivity. This is one of many difficulties that must be faced in order to achieve accurate temperature measurements in the EBAM process with an infrared camera. Radiation from the electrons requires that the viewport into the build area be shielded with leaded glass.

This glass causes transmission losses in the infrared spectrum. In order to capture images during the melting process the shutter must be opened which causes a metal film to be deposited on the surface of glass. This film causes further transmission losses. The emissivity of the target area is a critical parameter when converting radiant temperature to true temperature. Emissivity is dependent on surface condition, wavelength, temperature, and angle of incidence (González-Fernández et al., 2012) [9]. Because emissivity is dependent on so many factors, it can be a very difficult property to determine. Price et al. (2012) [10] evaluated a near infrared (NIR) thermal imager to measure temperature distributions and history of a build part surface during the EBAM process. It was shown that the NIR thermography, with a shorter spectral range, is able to capture temperature images of the preheating, contour melting, and hatch melting phases of the EBAM fabrication process. Moreover, the molten pool shape and size as well as an average molten pool temperature profile can be determined. A more detailed literature review and explanation of the experimental setup used in this paper may be found in Price et al. [10].

In this study, the repeatability of the 2D temperature profiles as well as a more thorough study of molten pool dimensions are presented. The emissivity of the molten pool and the transmission loss due to metallization were calculated, and the studies of build height and overhang effects were also conducted.

Experimental Setup

An Arcam S12 EBAM machine at NASA's Marshall Space Flight Center was used to build the test parts. Temperature measurements of the EBAM process were made with a LumaSense MCS640 NIR infrared camera. The NIR camera has a spectral range of 0.78-1.08 μm and a 640 x 480 pixel uncooled focal plane array (FPA) sensor. The image capturing system has a maximum frame rate of 60 Hz and a detectable temperature range of 600 to 3000 $^{\circ}\text{C}$ which is divided into three nominal ranges: low (735-1108 $^{\circ}\text{C}$), medium (1057-1485 $^{\circ}\text{C}$), and high (1503-2446 $^{\circ}\text{C}$). The camera has a lens with a minimal 500 mm working distance and a view area of 31 mm x 23 mm at 500 mm distance. The camera was calibrated with the glass in the viewport of the S12 EBAM machine so that a transmission rate of unity will correctly account for the transmission losses due to the glass. The powder material used was Ti-6Al-4V. The emissivity of the surface was unknown so measurements were taken with assumed emissivities of 0.35 and 0.5. The integration time of the image capturing system is 16.25 ms, 1.7 ms, and 50 μs for the low, medium, and high temperature ranges, respectively. The data acquisition system consisted of a laptop and an Ethernet cable, connected with a gigabit Ethernet express card.

The NIR camera was mounted on a tripod and positioned to look downward through the S12 EBAM machine's viewport onto the build platform. The camera was vertically inclined at 35 $^{\circ}$ from the surface normal with minimal roll angle and horizontal yaw. More detail on the experimental setup may be found in Price et al. (2012) [10]. The S12 EBAM machine contains a heat shield that is placed between the viewport and the build platform. This heat shield has a cutout for viewing the build platform but that cutout is obstructed with vertical bars. Three of these bars were cut to provide a clear view of the build platform, but interference from a single bar was still observed during testing. Several parts of different geometries were fabricated in order to study a variety of effects. Simple rectangular cross-sections were employed in order to study hatch melting and overhang structures were used to study melting over a powder substrate.

Results and Discussion

A. Near Infrared Imaging of the EBAM Process

The different temperature ranges of the NIR camera are each uniquely suited for imaging the various stages of the fabrication process. The low temperature range is best suited for preheating, the medium temperature range for contour melting, and the high temperature range for hatch melting. Examples of NIR images of the various portions of the EBAM process are shown in Figure 1. The images are from the fabrication of a 30.48 mm x 25.4 mm solid cross-section.

The spatial resolution of the NIR images was determined by identifying the edges of the part during the contour melting phase, then determining the number of pixels between these edges. The average horizontal and vertical spatial resolutions of the images were found to be 46.8 $\mu\text{m}/\text{pixel}$ and 66.2 $\mu\text{m}/\text{pixel}$ respectively. The vertical spatial resolution is larger due to distortion caused by the 35° tilt of the camera.

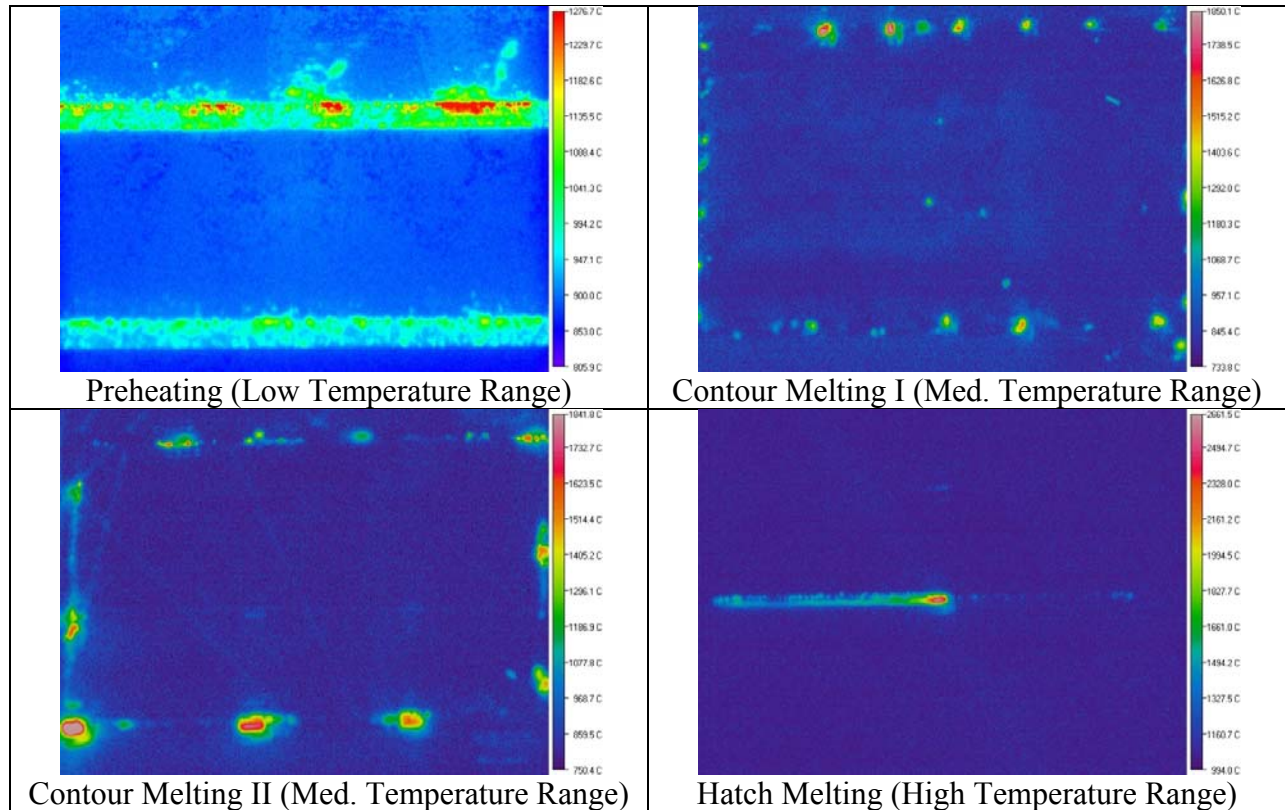


Figure 1. NIR images of the various stages of the EBAM fabrication process.

B. Repeatability of Temperature Measurements

The repeatability of the temperature measurements was also examined. This was accomplished by creating 2D temperature profiles along the scan path of each frame and averaging these profiles together. The average 2D temperature profile of the hatch melting of a single layer with standard deviations is shown below in Figure 2. For this particular layer, the

electron beam scanned back and forth horizontally. Temperature profiles of leftward scans were flipped to be rightward and all the profiles were aligned at their peak temperatures to correctly line up the profiles for averaging. The temperature profile appears to be very repeatable, especially in the high temperature region around the beam location.

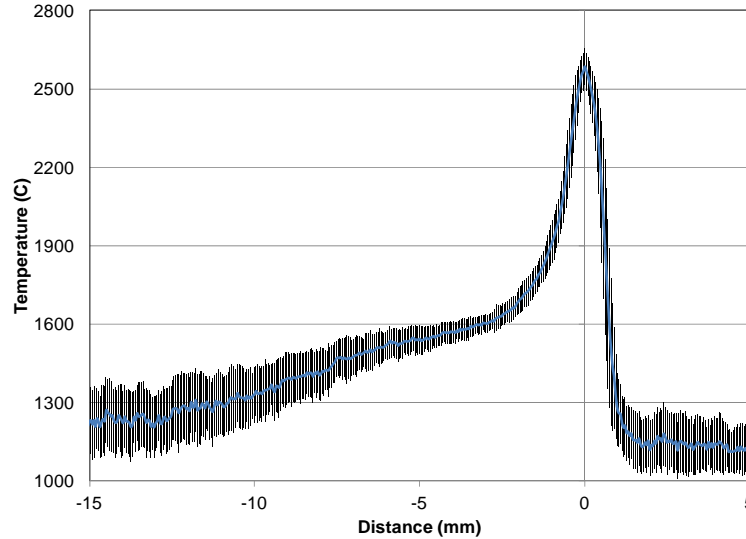


Figure 2. Average hatch melting temperature profile from a single layer.

Average temperature profiles were made for four different layers over a ten layer range (0.7 mm range) and compared together in order to study the repeatability of the temperature measurements over multiple layers. These profiles are shown in Figure 3 and it may be seen that the temperature profiles match almost identically. Layer 17's temperature profile shows a plateau slightly above 1800 °C where the peak should be found. This occurred because the footage of this layer was captured using the medium temperature range of the camera. The plateau occurs at that the maximum detectable temperature of the medium temperature range.

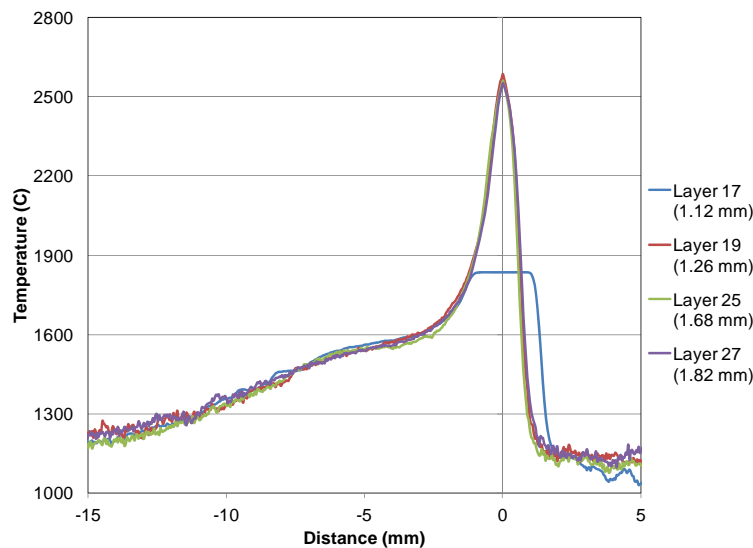


Figure 3. Average profiles showing the repeatability of the temperature measurements.

C. Build Height Effects

The effect of build height on the thermal behavior of the powder during hatch melting was investigated. An average 2D temperature profile along the scanning path was generated for each recorded build height and then compared in Figure 4 to identify trends. The horizontal distance from the peak temperature to the solidus temperature on the cooling side of the profile is shorter at higher build heights; however the location of liquidus temperature does not appear to vary with build height. A suspected cause for the change in horizontal location of the solidus temperature is higher beam speeds and currents used by the Arcam S12 machine in the initial layers of the build. These results show that build height may have very little effect on the thermal characteristics of the EBAM process.

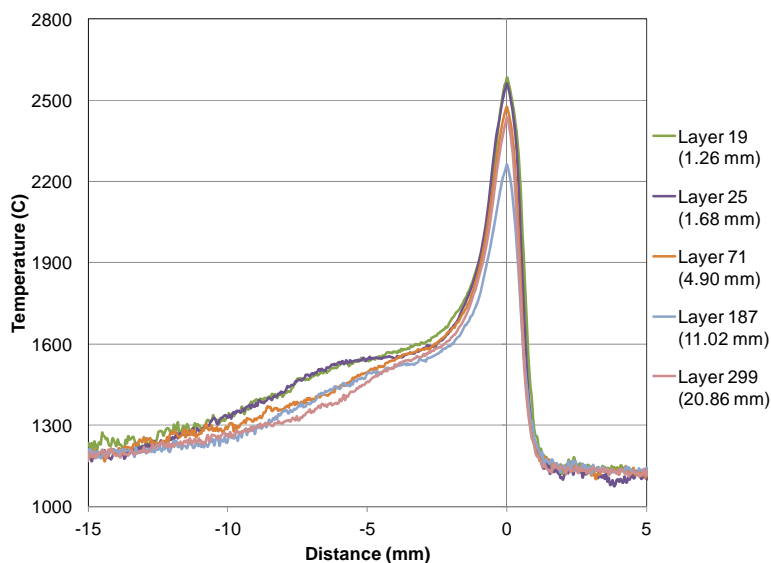


Figure 4. Temperature profiles across the molten pool at various build heights.

D. Transmission Loss due to Metallization of Sacrificial Glass

During the fabrication process, some of the Ti-6Al-4V powder gets evaporated and forms a thin layer on the interior of the viewport. A piece of sacrificial glass shields the thick, protective glass in order to protect it from the metallization. This glass can be easily discarded and replaced after it becomes obscured by the metal film. The sacrificial glasses from several of the experiments were salvaged and tested in order to determine the severity of the transmission loss caused by the metallization. The sacrificial glass used in the experiment that generated all the data for this paper except the overhang study is shown below in Figure 5. The transmission losses were determined by the following experimental procedure. The NIR camera was used to image a tungsten filament with a clear sacrificial glass between the two. The average temperature of the filament was then determined. Next, the darkened sacrificial glass from the experiment was placed in between the camera and the filament and the average measured temperature of the filament was determined for multiple transmission rates. The true transmission rate was found by selecting the one that provided the filament temperature closest to the one measured with the clear glass. The transmission loss from the metallization of the

glass alone in air shown in Figure 5 was found to be about 20% and the transmission loss due to the leaded and vacuum glasses has been measured to be 47%. The total transmission loss caused by the metallization is about 9.4% and this was found by multiplying the two transmission losses together.

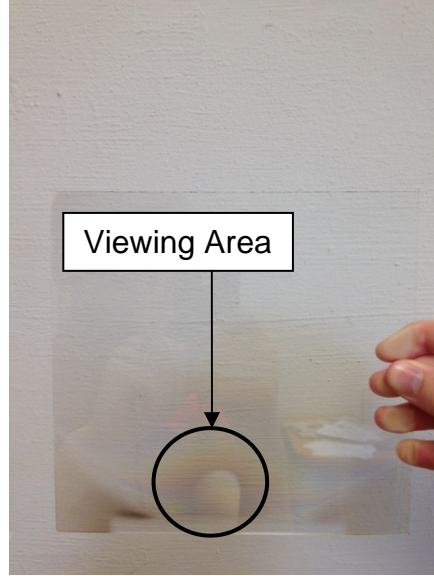


Figure 5. Sacrificial glass with metallization.

E. Molten Pool Emissivity

The emissivity of the molten pools was estimated by determining the measured value of the liquidus temperature on the 2D temperature profile then calculating the emissivity required to convert the measured liquidus temperature to Ti-6Al-4V's true liquidus temperature (1655 °C). The following equation from Whintont (2010) [11] was used to calculate the emissivity:

$$M = \left[\int_{\lambda_1}^{\lambda_2} \frac{w_\lambda}{\lambda^5 \left(\frac{c_2}{e^{\lambda T_{app}}} - 1 \right)} d\lambda \right] - \left[\varepsilon \int_{\lambda_1}^{\lambda_2} \frac{w_\lambda}{\lambda^5 \left(\frac{c_2}{e^{\lambda T_{true}}} - 1 \right)} d\lambda \right] - \left[(1 - \varepsilon) \int_{\lambda_1}^{\lambda_2} \frac{w_\lambda}{\lambda^5 \left(\frac{c_2}{e^{\lambda T_{envir}}} - 1 \right)} d\lambda \right] \quad (1)$$

where,

- M = a variable to minimize by adjusting other variables,
- λ_1 = bottom of infrared camera's spectral range in μm ,
- λ_2 = top of infrared camera's spectral range in μm ,
- λ = wavelength of light in μm ,
- w_λ = relative sensitivity of camera at wavelength λ ,
- c_2 = second radiation constant (14388 $\mu\text{m} \cdot \text{K}$),
- T_{app} = apparent temperature in K,
- T_{true} = true temperature in K,
- T_{envir} = surrounding environment temperature in K, and
- ε = emissivity.

The measured liquidus temperature was used as the true temperature and the assumed emissivity value input into the camera was used as the emissivity. The relative sensitivity of the camera at λ was assumed to be unity because this information was not available from the camera manufacturer. The equation was numerically solved for a range of apparent temperatures. The apparent temperature that resulted in the smallest value of M was the correct value. Using the calculated temperature as the apparent temperature and the liquidus temperature of Ti-6Al-4V for the true temperature, the equation was numerically solved again, this time looking for the emissivity that resulted in the smallest value of M.

The average molten pool emissivities and their standard deviations were calculated at various build heights and are shown in Figure 6. The grand mean is represented by the solid red line and the standard deviation of the averages is represented by the dashed red lines. The grand mean was found to equal 0.283 and the standard deviation 0.018. Boivineau et al. (2006) [12] found the emissivity of Ti-6Al-4V to be around 0.58 at the liquidus temperature where it then drops to 0.4 in its liquid state. The emissivity they found was the normal spectral emissivity of Ti-6Al-4V at a spectral wavelength of 684.5 nm. The NIR camera employed in the current study was sensitive in the 780 nm to 1080 nm range, this might explain the difference in calculated emissivities since emissivity is a wavelength dependent property.

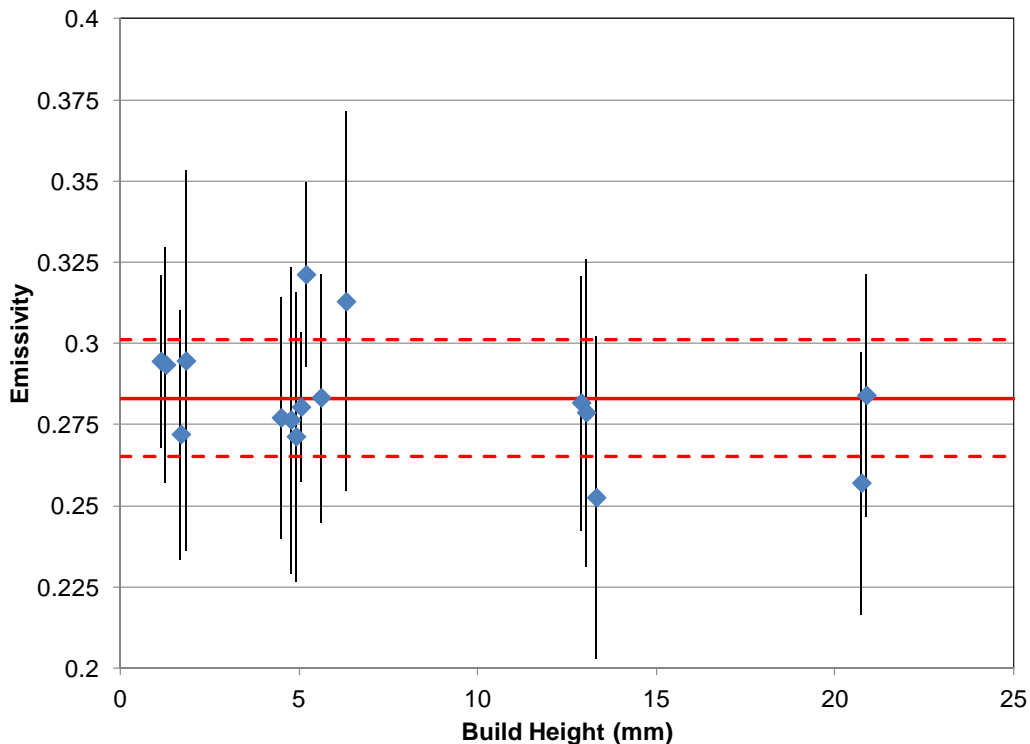


Figure 6. Average molten pool emissivities with standard deviations at various build heights.

F. Molten Pool Dimensions

The average length and width of the molten pool were also determined at various build heights. These dimensions were found by generating and measuring an isotherm at the measured liquidus temperature. An example post-processed image of a molten pool during hatch melting

is shown in Figure 7. The temperatures of the white pixels are equal to or greater than the liquidus temperature. The average molten pool dimensions are shown in Figure 8. The grand means of the molten pool average lengths and widths were 2.73 mm with a standard deviation of 0.16 mm and 0.98 mm with a standard deviation of 0.13 mm, respectively.

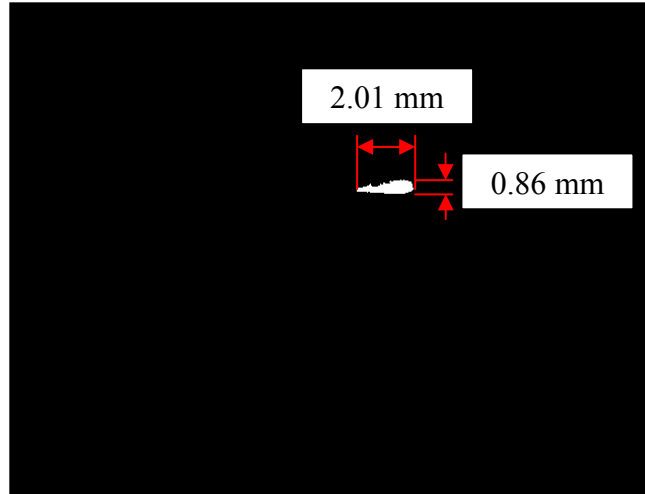


Figure 7. Post-processed NIR image showing size and shape of molten pool.

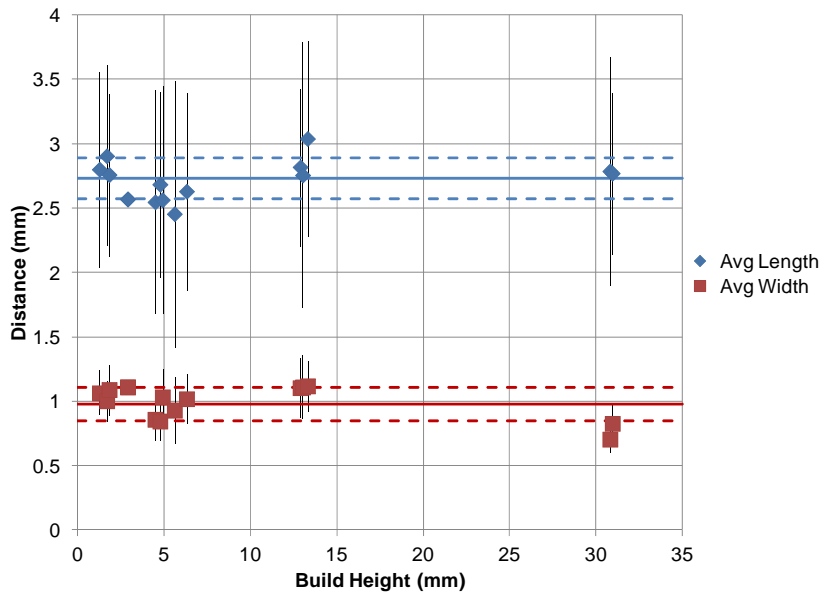


Figure 8. Average molten pool dimensions with standard deviations at various build heights.

G. Overhang Structure Thermal Effects

The thermal effects of melting over a powder substrate were also investigated in order to better understand this common scenario. A powder substrate is encountered during the build process because the powder serves as support material under overhang features of the part. The images shown in Figure 10 are from the fabrication of the middle “shelf” of the part shown in Figure 9. The top-right quarter of each image in Figure 10 has a solid substrate and the bottom-

right quarter of each image has a powder substrate. The images from the first overhang layer show that cooling occurs much slower over the powder substrate when compared with the solid substrate. However, this effect is almost completely diminished by the third layer above the powder substrate. In order to study the slower cooling over the powder substrate 2D temperature profiles were generated from frames from the first overhang layer footage. The profiles were aligned at the interface of the solid and powder substrates and oriented so that the common scanning direction was rightward, then averaged together. 2D temperature profiles were generated parallel to the scanning path at intervals of 2 mm out to 8 mm in order to show the cooling effect. The left image in Figure 11 shows an example of the locations of these temperature profiles and the right image shows the average temperature profiles. At 8 mm from the scan path, the part has almost cooled to the same temperature as the surrounding area. The dashed red boxes represent the regions that have a solid substrate.

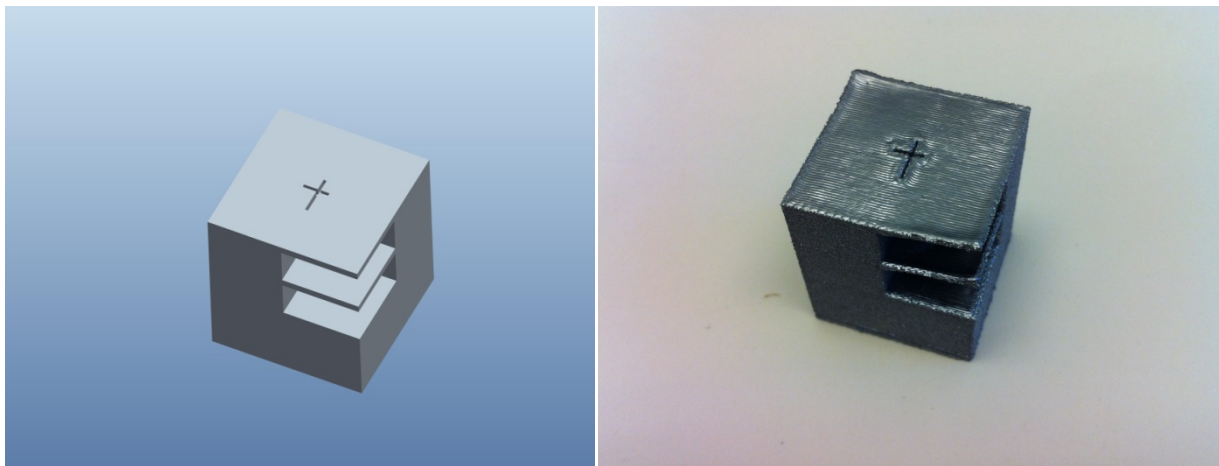


Figure 9. Overhang model and part fabricated during EBAM testing.

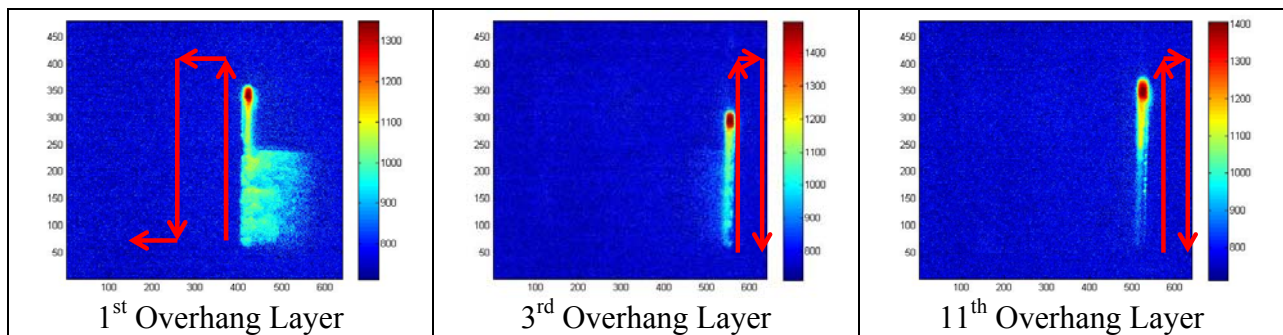


Figure 10. Temperature maps showing hatch melting over a half powder-half solid substrate.

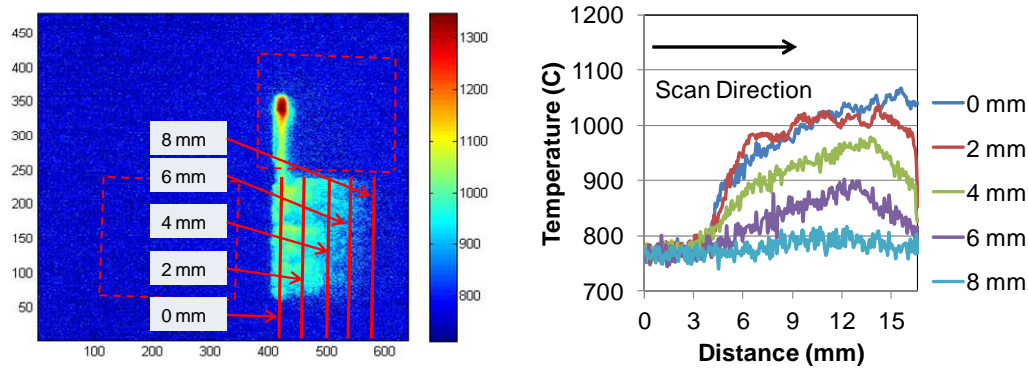


Figure 11. Average temperature profiles from first overhang layer.

Conclusions

An NIR camera has been used to make temperature measurements during an EBAM process. A part was built by the EBAM process that was designed to enable the observation of electron beam melting over a powder substrate. The effects build height has on various thermal characteristics of the electron beam melting process have been evaluated. The emissivity and dimensions of the molten pool were also determined at various build heights. Major conclusions from this research are listed below.

- 2D temperature profiles show that temperature measurements of the EBAM process with an NIR camera are repeatable.
- Build height may have very little effect on the thermal characteristics of the EBAM process, though some effect on the length of the liquidus-solidus transition region.
- Metallization of the viewport during fabrication leads to increased transmission losses through the viewport.
- The calculation of the molten pool emissivity is very sensitive to the measured liquidus temperature.
- The melting of the first layer over a powder substrate shows a significantly decreased cooling rate when compared to cooling over a solid substrate.
- Future work will compare experimental data with simulation results in order to validate process models as well as to study process parameter effects on the thermal characteristics of the EBAM process.

Acknowledgement

This research is supported by NASA, No. NNX11AM11A and is a collaboration between The University of Alabama and MSFC. Support from Majid Babai, Chief of Nonmetallic Branch at MSFC, is greatly appreciated.

References

- [1] Gong, X., Anderson, T., Chou, K., 2012, "Review on Powder-Based Electron Beam Additive Manufacturing Technology," ASME 2012 International Symposium on Flexible Automation, St. Louis, MO, June 18-20, 2012 (ISFA2012-7256).
- [2] Záh, M. F., Lutzmann, S., 2010, "Modelling and Simulation of Electron Beam Melting," *Production Engineering*, 4(1), pp. 15-23.
- [3] Qian, L., Mei, J., Liang, J., Wu, X., 2005, "Influence of position and laser power on thermal history and microstructures of direct laser fabricated," *Materials Science and Technology*, 21, pp. 597-605.
- [4] Wegner, A., Witt, G., 2011 "Process Monitoring In Laser Sintering Using Thermal Imaging," SFF Symposium, Austin, TX, 2011, pp. 405-414.
- [5] Craeghs, T., Clijsters, S., Yasa, E., Bechmann, F., Berumen, S., Kruth, J. P., 2011, "Determination of geometrical factors in Layerwise Laser Melting using optical process monitoring," *Optics and Lasers in Engineering*, 49, pp. 1440-1446.
- [6] Wang, L., Felicelli, S. D., Craig, J. D., 2009, "Experimental and numerical study of the LENS rapid fabrication process," *Journal of Manufacturing Science and Engineering*, 131, pp. 1-8.
- [7] Schwerdtfeger, J., Singer, R. F., Körner, C., 2012, "In situ flaw detection by IR-imaging during electron beam melting," *Rapid Prototyping Journal*, 18(4), pp. 259-263.
- [8] Rodriguez, E., Medina, F., Espalin, D., Terrazas, C., Muse, D., Henry, C., MacDonald, E., Wicker, R., 2012, "Integration of a Thermal Imaging Feedback Control System in Electron Beam Melting," WM Keck Center for 3D Innovation, University of Texas at El Paso, pp. 945-961.
- [9] González-Fernández, L., Risueño, E., Pérez-Sáez, R.B., Tello, M. J., 2012, "Infrared Normal Spectral Emissivity of Ti-6Al-4V Alloy in the 500-1150 K Temperature Range," *Journal of Alloys and Compounds*, 541, pp. 144-149.
- [10] Price, S., Cooper, K., Chou, K., (2012), "Evaluations of Temperature Measurements by Near-infrared Thermography in Powder-based Electron-beam Additive Manufacturing," 23rd Annual International Solid Freeform Fabrication Symposium, Austin, TX, Aug. 6-8, 2012.
- [11] Whitenton, E., 2010, "High-Speed Dual-Spectrum Imaging for the Measurement of Metal Cutting Temperatures," US Department of Commerce, National Institute of Standards and Technology.
- [12] Boivineau, M., Cagran, C., Doytier, D., Eyraud, V., Nadal, M.-H., Wilthan, B., Pottlacher, G., (2006), "Thermophysical Properties of Solid and Liquid Ti-6Al-4V (TA6V) Alloy," *International Journal of Thermophysics*, 27(2), pp. 507-529.